

On the efficiency of rotational-vibrational Raman spectroscopy methods in laser sensing of the cloudy atmosphere

G.M. Krekov and M.M. Krekova

*Institute of Atmospheric Optics,
Siberian Branch of the Russian Academy of Sciences, Tomsk*

Received February 7, 2005

The Monte Carlo numerical experiment has been used to study the efficiency of rotational-vibrational Raman spectroscopy during laser sensing of temperature and humidity in the atmosphere. In the real atmosphere, the main source of active noise, limiting the potential capabilities of a lidar, is multiple scattering of a laser signal by aerosol and cloud particles. Under the lower- and middle-level overcast conditions, the Raman lidar is inapplicable. It is an urgent problem to estimate the limits of the Raman sensing applicability in the presence of aerosol inversions and invisible upper-level cirrus clouds. In this paper, we estimate a possible shift of vertical profiles of temperature, humidity, and the ratio of H₂O vapor mixture due to the multiple scattering noise in the recording channel for cases of ground-based and orbital sensing. The boundary conditions of the problem correspond to those of the most efficient active lidars of the European lidar network, using the signals of purely rotational and rotational-vibrational Raman scattering induced by the pulsed Nd:YAG laser radiation at a wavelength of 532.25 nm. The estimates confirm the promises of applying the methods of rotational-vibrational Raman spectroscopy to sensing the temperature in a height range 2–20 km, while the errors in estimation of water vapor profiles achieve 10–15%.

Introduction

Today, one of the methods to timely provide information about the Earth's atmosphere state is a remote laser sensing. Traditionally, laser sensing is based on interpreting the spatially resolved signal of the elastic scattering in a medium under study at one or several frequencies of the optical wavelength region.¹

In the last decade, there has been formed a natural tendency to use a broad range of linear and nonlinear processes resulting in re-emission at other frequencies by the matter of the sensed medium (so-called trans-spectral processes).^{2–4} In this paper, we pay special attention to analysis of noise-resistance of optical laser lidars that use Raman signals in the atmospheric sensing (Raman lidars).⁵ When properly applied, Raman lidars give a regular information on spatial distribution of the majority of basic atmospheric parameters essential for the analysis and prognosis of air basin behavior up to the cirri.

Systematic results, as they are gradually accumulated, are analysed by the European aerosol lidar network (EARLINET)⁶ and Siberian Lidar Station.⁷ These results concern first of all the study of the long-term time series of vertical profiles of humidity, temperature, and ozone concentration. Analysis of this data allows one to judge on the influence of dynamics of strong atmospheric fronts,⁸ volcanic eruptions,⁹ technogenic emissions,¹⁰ and other impacts disturbing the ecosystem. Combination of the Raman lidar with multifrequency elastic scattering lidars^{11,12} allows researchers to obtain the information

on vertical variations of the atmospheric aerosol microstructure of both background and anthropogenic character.

A special type of inverse problems of optical sensing appears in Raman diagnostics of the above parameters in the cloudy atmosphere. The low-level overcast makes it impossible to apply the Raman lidar. At the same time, optically thin cirrus clouds are the object of growing interest of specialists in the field of both passive and active sensing.¹³ The reason is in the important role of cirrus clouds (even invisible ones) in the Earth's radiation regime.¹⁴ They also are an active noise source for space-based optical sensors.¹⁵ In turn, the formation processes and microphysical properties of cirrus clouds are strongly conditioned by the temperature stratification dynamics in the troposphere and lower stratosphere.¹⁶

In this connection, we tried to quantitatively estimate the efficiency of the Raman spectroscopy methods in laser sensing of two main interrelated meteorological parameters of the atmosphere, namely, temperature and humidity in conditions of the surface atmosphere excess turbidity and tropopause cirri.

Raman sensing of vertical temperature profiles

At present, methods of laser sensing of temperature profiles $T(h)$ are extremely diverse. A rather complete comparative analysis of the methods can be found in Refs. 7, 15, 17, 18. In the last decade, the leading upper-air laser sensing stations^{7,12,19}

including the European lidar network, prefer the methods of rotational Raman spectroscopy (RRS) due to much larger backscattering cross sections. The formerly important problems of selecting desired signals in the region of the *O*- and *S*-branches of pure rotational Raman spectrum near the excitation frequency are successfully solved by new methods.^{19–21} In turn, the methods, in which the scattering RRS is used, can lean upon a) comparison of frequency shift of the RRS band intensity maximum, b) analysis of envelope profile of the curve of interest, c) analysis of ratio of the Stokes and anti-Stokes RRS intensity components, etc. In particular, in results of our early studies^{22,23} reflected in the equipment developed for the Central Aerological Observatory,²⁴ we suggested the method of separation of molecular and aerosol scattering components and reconstruction of the temperature profile by using the signals in the RRS line series and the elastic scattering signal at the excitation frequency. The method is based on the iterative algorithm of solving the resulting system of lidar equations. Estimations showed a possibility of $T(h)$ reconstruction from the RRS signal of molecular nitrogen with excitation by the third harmonic of a ruby lidar ($\lambda_0 = 694.3$ nm). Simultaneously, at the Institute of Atmospheric Optics, the method suggested by Cooney²⁷ was improved and implemented. Below, we will dwell on potentialities of this method, which uses the ratio of backscattering intensities in two RRS spectral bands with opposed temperature dependence.

Usually, to determine the rotational gas temperature T , we use the line intensity of only the *O*- and *S*-branches of $v \rightarrow v$ vibrational band for the single-component gases and $v \rightarrow v + 1$ band for the multicomponent gas mixtures (v is the vibrational quantum number). Selection criteria for the Raman scattering transitions of the biatomic and linear molecules of the atmospheric nitrogen type have the form

$$\Delta v = 0, \pm 1 \text{ and } \Delta J = 0, \pm 2,$$

where J is the rotational quantum number. According to the Placek polarization theory,^{17,28,29} the differential cross section of spontaneous Raman backscattering for the vibrational-rotational *O* and *S* transitions is determined by the following expression:

$$\frac{d\sigma_R}{d\Omega} = \frac{(2\pi)^4}{45} \frac{b^2(v_0 - v)^4}{1 - \exp(-h\nu c/kT)} g(45\alpha_0^2 + 7\gamma_0^2), \quad (1)$$

where v_0, v are the excitation and shifted frequencies, respectively; b stands for the molecular vibration amplitude $b = h/(8\pi^2\nu c)$; g is the degeneration degree; α_0^2 and γ_0^2 are isotropic (average) and anisotropic parts of the polarizability tensor derivative. Other symbols have their commonly accepted physical meaning. For the pure RRS, cross section shape in Eq. (1) is simplified, because the factor

$$\frac{b^2 g}{1 - \exp(-h\nu c/kT)} \approx 1 \quad (2)$$

and almost coincides with the Cabannes–Rayleigh scattering. Here, α_0^2 and γ_0^2 are taken for $\Delta v = 0$.

Thus, band-cumulative cross section of the pure RRS does not contain information on the temperature gradient. At the same time, intensity of individual RRS lines is considerably T dependent. It follows, for example, from Refs. 29 and 30, that relative intensity of the normalized RRS

$$I_R(J, T) = C v_J^4 q_J S_J F_\gamma(m) \times \exp\left\{-\frac{hc}{kT} [B_J J(J+1) - D_J J^2(J+1)^2]\right\}, \quad (3)$$

where C is the normalization constant;

$$v_J = v_0 \pm 4B_J(J + 3/2)$$

is the RRS line frequency; q_j stands for the statistical weight conditioned by the nuclear spin; B_i and D_i are the effective rotational constants; $F_\gamma(m)$ is the vibrational-rotational interaction factor for the matrix element of polarizability³⁰ with $m = 2J + 3$ for the *S*-branch and $m = -2J + 1$ for the *O*-branch; S_j is the Planck–Teller coefficient of the form

$$\begin{cases} S_{J \rightarrow J+2} = \frac{3(J+1)(J+2)}{2(2J+1)(2J+3)}, \\ S_{J \rightarrow J-2} = \frac{3J(J+1)}{2(2J+1)(2J-1)}. \end{cases} \quad (4)$$

It has been shown³⁰ that Eq. (4) being T -dependent, can be simplified by assuming $F_\gamma(m) = 1$ and $D_j = 0$. For the RRS of N_2 and O_2 this leads to the error within 1–3 K. With this assumption, the determination procedure for T is reduced to measurements, for example, of the line intensity in *S*-branch with $J = 0 - J_{\max}$ or $J = 0, 2, 4, \dots, J_{\max}$, and solution of the resulting equation system of type (3). In practice, realization of such measurements imposes unrealistic demands on spectral resolution and calibration accuracy. Under the same assumptions, as it is pointed out in some works (Refs. 19–21, for example) it is more reasonable to take the backscattering intensity ratio of two allowed transitions, for example, J_1 and J_2 , as the functionals to be measured. They are located in the *S*- or *O*-branch segments of the pure RRS with different dI/dT gradient signs, i.e., in the region of small and large quantum numbers J . In this case, we obtain a simple functional temperature dependence of the form

$$R(T) = \frac{I_R(J_1, T)}{I_R(J_2, T)} = \exp\left[\frac{\gamma}{T} + \chi\right], \quad (5)$$

where

$$\chi = \ln S_J(J_1) - \ln S_J(J_2); \quad \gamma = E_J(J_2) - E_J(J_1)/k;$$

E_J is the rotational energy, which can be approximated²⁰ by the equation $E_J = J(J+1)hcB_J$. When implementing this approach by laser sensing

techniques, relation (5) will correspond to the ratio of the Raman backscattering signals in two specified spectral regions Δv_1 and Δv_2 , i.e.,

$$R(T, h) = \frac{P(h, \Delta v_1)}{P(h, \Delta v_2)}, \quad (6)$$

where h stands for the sensing range.

The values of the received signals $P(h, \Delta v)$ must meet the single scattering requirement, i.e., satisfy in a certain approximation to the laser location equation, which involves the temperature dependence^{5,22}

$$P(h, v) = P(v_0) C_R(h) \frac{\beta_R(h, v)}{h^2} \times \exp \left\{ - \int_0^h [\sigma(h', v_0) + \sigma(h', v)] dh' \right\}, \quad (7)$$

where $P(h, v)$ is the power received from the h distance at the Raman frequency v ; $P(v_0)$ is the emitted lidar power; $C_R(h)$ is the instrumental factor including the overlapping function; σ stands for the total coefficient of the atmospheric extinction at the elastic (v_0) and inelastic (v) scattering frequencies, respectively, km^{-1} ; β_R is the Raman backscattering coefficient, km^{-1} . Approximation character of Eq. (7) consists in the following. If the atmospheric sensing channel contains N_X molecules, cm^{-3} , of X type and the detection is realized in a small finite spectral interval Δv , then

$$\begin{aligned} \beta_R[h, \Delta v, T(h)] &= N_X(h) \int_{\Delta v} \frac{d\sigma_R[v', T]}{d\Omega} \xi(v') dv' = \\ &= N_X(h) F_R[T(h)] \frac{d\sigma_R}{d\Omega} \xi(v_X), \end{aligned} \quad (8)$$

where

$$F_R[T(h)] = \frac{\int [d\sigma_R[v', T(h)] / d\Omega] \xi(v') dv'}{[d\sigma_R / d\Omega] \xi(v_X)}; \quad (9)$$

$\xi(v)$ is the transmission efficiency of the selective filter within the Δv band at the frequency $v \in \Delta v$, v_X being the RRS frequency of molecules of X type. In Ref. 5, D. Whiteman shows that the function $F_R[T(h)]$, including the temperature dependence, at an appropriate filter window is practically invariable in the altitude interval $h = 0.5\text{--}15$ km for molecules O_2 , N_2 , and H_2O . Hence, for practical applications, it is tolerable to assume in Eq. (8) $\beta_R(h) \approx N_X(h) \frac{d\sigma_R}{d\Omega}$.

Model estimates of $T(h)$ in the background multiple scattering conditions

The estimate of vertical temperature profile by the backscattering RRS immediately follows from Eq. (5)

$$T_0(h) = \frac{\gamma}{\ln R_0(h) - \chi}. \quad (10)$$

It is implied that

$$R_0(h) = P_0(h, v_1) / P_0(h, v_2),$$

where $P_0(h, v_1)$ and $P_0(h, v_2)$ are the single scattering signals, and the atmospheric transmission in the sensing channels at the RRS frequencies v_1 and v_2 is strictly equal. Under real atmospheric conditions, especially cloudy ones, both these requirements need a critical analysis. The effects of the secondary elastic scattering at the working frequencies v_1 and v_2 lead to the following: the detector receives the radiation, whose intensity is determined from solution of the complete transfer equation in the boundary conditions reflecting the experimental scheme. Then Eq. (10) takes the following form for the temperature profile shifted due to multiple scattering noise:

$$T(h) = \frac{\gamma}{\ln [R_0(h) \eta(h)] - \chi}, \quad (11)$$

where

$$\eta(h) = \frac{I(h, v_1) / I(h, v_2)}{I_0(h, v_1) / I_0(h, v_2)}; \quad (12)$$

$I_0(h, v)$ and $I(h, v)$ are solutions of transfer equation for the single and complete scattering signal intensity (accounting for all multiplicities of the elastic photon interaction) at the shifted Raman frequency v .

In this numerical experiment, temporal behavior of $I(h, v_1)$ and $I(h, v_2)$ is calculated for the monostatic sensing scheme of the Raman lidar operating at $\lambda_0 = 532.25$ nm (the second harmonic of the Nd:YAG laser). The total divergence angle for the source $\varphi_t = 0.1$ mrad, and the total sight angle of the receiving telescope varied within $\varphi_d = 0.2\text{--}1$ mrad. It was supposed also that the interference filter of the receiving system cuts off spectral regions around $\lambda_2 = 529.25$ and $\lambda_2 = 531.35$ nm. The enumerated parameters of the ground-based lidar are close to those of one of the European network lidars.^{6,20} For orbital calculations,³² the same parameters of the transmitting-receiving lidar system were supposed.

Optical characteristics of the atmosphere in model calculations are the piecewise-constant functions of the altitude h . The atmosphere is cut into layers with uneven step $\Delta h_i = h_{i+1} - h_i$, $i = 1, 2, \dots, n_h$ (with a finer step within a cloud). In each layer Δh_i , the scattering phase function and the model values of optical molecular and aerosol interaction coefficients are specified, using the data of Refs. 1 and 33, as well as the temperature, mixing ratio, and partial pressure of H_2O vapor by the data of Ref. 34. Optical characteristics of the cloud composed of chaotic hexagonal medium-sized columns can be found in Ref. 35.

The strict approach to the problem of the Raman radiation transfer in a turbid atmosphere is connected with solution of a multigroup transfer equation. The Monte Carlo solution was discussed by us in detail in

Ref. 4. It was noted that the closeness of the spectral intervals $\Delta\nu_1$ and $\Delta\nu_2$, in which we estimate the desired functionals after solution of the transfer equation, undoubtedly requires the use of the method of correlated samples.^{4,36}

On the whole, the Raman signal calculations in the cloudy atmosphere, taking into account multiple scattering, are few in number,^{4,37–40} while their results are extremely contradictory. In Fig. 1, we give some available model estimates in the form of the multiple scattering factor

$$F_M(h) = \frac{P^{MS}(h)}{P^{SS}(h)}, \quad (13)$$

where $P^{SS}(h)$ is the signal of inelastic single Raman scattering, $P^{MS}(h)$ is multiply scattered signal component conditioned by all interaction types. Most calculations, including ours, are carried out for the ground-based lidar with the aperture angle $\phi_t = 0.1$ mrad and the total receiving angle $\phi_d = 0.4$ mrad. Estimates are obtained for the commonly available C1 model⁴¹ of the cloud at the altitude $h_0 = 5$ km, having the thickness $\Delta h = 200$ m, and optical density $\sigma = 10 \text{ km}^{-1}$.

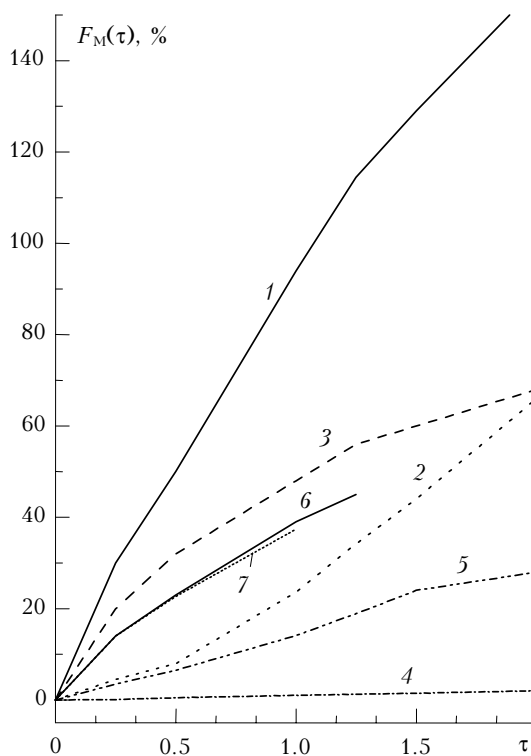


Fig. 1. Comparison of test calculations of the multiple scattering factor $F_M(\tau)$ with data of other authors: the results obtained in Ref. 37 and our calculations for the cloud model at the altitude of 5 km, $\lambda_0 = 308$ nm, $\sigma = 10 \text{ km}^{-1}$ (curves 1, 2); the results of Refs. 38, 40, and our calculations for the same cloudiness model, $\lambda_0 = 532$ nm (curves 3, 4, 5); the results of Ref. 39 and ours for the model of a crystalline cloud at the altitude $h = 7\text{--}10$ km, $\lambda_0 = 355$ nm, $\sigma = 0.6 \text{ km}^{-1}$ (curves 6, 7).

It is seen that the factor $F_M(\tau)$ varies widely by different estimates. Maximal values (curve 1) were

obtained³⁷ by the approximate analytical method at $\lambda_0 = 308$ nm. The smallest values for $F_M(\tau)$ were obtained³⁸ by Monte Carlo calculations (curve 4) at $\lambda_0 = 532$ nm. The relative multiple scattering does not exceed 2% over the whole sensing channel. Curve 3 is built up according to Ref. 40, where calculations were performed at $\lambda_0 = 532$ nm.

Our estimates are intermediate. Curves 2 and 5 are calculated, respectively, for $\lambda_0 = 308$ and 532 nm; quantitative behavior of $F_M(\tau)$ obtained by us well agrees with similar results from Ref. 42, as well as with the results obtained for the case of elastic scattering and generalized in Ref. 43. The results by J. Reichardt (Ref. 40) obtained for the crystalline cloud model at $\lambda_0 = 355$ nm (curve 6) are the closest to our estimates (curve 7).

One of possible reasons of the divergence between the results shown in Fig. 1 is the fact that many authors disregard distinctions between Rayleigh and Raman scattering phase functions. Other possible reasons of distortions of the Raman signal under the multiple scattering conditions are discussed in detail in Ref. 4.

Further we discuss the effect of the Raman signal's background component on the temperature profile reconstruction when sensing the atmosphere in the presence of optically thin crystalline clouds. We consider different variations of optical state of the subcloud atmosphere and the crystalline cloud.

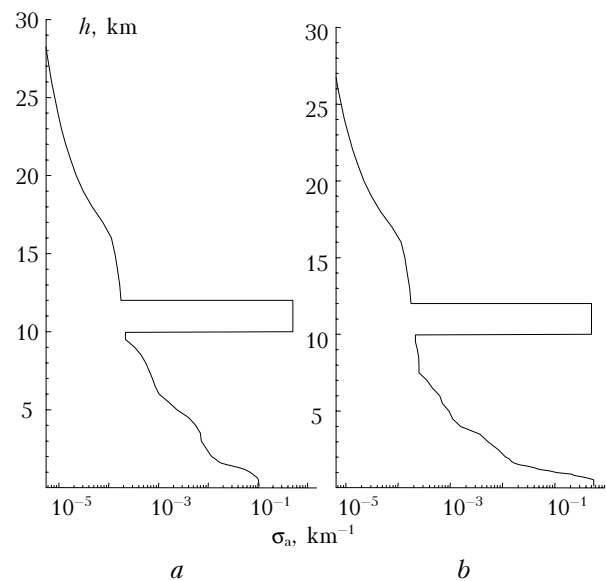


Fig. 2. Aerosol extinction coefficient profiles used in the model calculations. Aerosol profile $\sigma_a(h)$ in the subcloud atmospheric layer corresponds to: background model³³ (a); fog (b).

Figure 2 shows profiles of the aerosol and cloud extinction coefficients in a 30-km-thick atmospheric layer, used by us in calculation estimates. Two variants of the subcloud atmosphere are considered: the background aerosol³³ and the fog with the profile decreasing with altitude. Spectral behavior of the aerosol extinction coefficients $\sigma_a(\nu)$ in the visible

spectral region is tolerably approximated by the Angström law³³

$$\sigma_a(v) = \sigma_a(v_0) \left(\frac{v_0}{v} \right)^{-\gamma_\Lambda} \quad (14)$$

with the colour grade index $\gamma_\Lambda \approx 1.0$. For simplicity, we suggest the same dependence for the spectral behavior of the aerosol backscattering coefficient, though ambiguity of this assumption needs a further analysis.

The cirrus cloud layer is located at the altitudes of 10–12 km above the Earth's surface. Figure 3 shows statistical modeling results that determine the limits of possible temperature profile shift due to multiple scattering noise in the Raman channel at $\lambda_1 = 530.3$ and $\lambda_2 = 535.1$ nm.⁴⁴

Calculations are performed for a set of total receiving angles $\varphi_d = 0.2, 0.4, 0.6, 1.0$ mrad.

Figure 3a illustrates the temperature profile reconstruction error $\Delta T(h)$ in absolute units for the clear atmospheric subcloud layer. As the optical cloud model, we used characteristics calculated for small hexagonal columns of $50/10 \mu\text{m}$.³⁵ Note that the reconstructed temperature profile shift with respect to the model profile occurs only due to disagreement between the signal levels including their background components registered in the channels at λ_1 and λ_2 .

Qualitative behavior of $\Delta T(h)$ agrees with the $F_M(h)$ function shape (see Ref. 4, Fig. 3). Reconstruction error for $T(h)$ including the cloud layer is less than 0.1° . Beyond the cloud, the value of $\Delta T(h)$ grows and reaches its maximum at distances comparable to cloud's length. This is characteristic of the $F_M(h)$ maximum formation, which is due to a strong aftereffect of the upper cloud layer onto the

temporal signal behavior. With the increase in φ_d aperture, the $T(h)$ reconstruction error grows as well and reaches $2\text{--}3^\circ$ beyond the cloud layer. For $\varphi_d < 1$ mrad, $\Delta T(h)$ tends to decrease in direction to the top boundary of the sensed atmospheric layer.

Figure 3b shows an example of calculating $\Delta T(h)$ for subcloud mist conditions (optical properties of the mist correspond to data in Fig. 2b). The presence of mist promotes the growth of the temperature reconstruction error in the cloud layer up to $\sim 0.5\text{--}1^\circ$ depending on the receiving aperture. Compared to the previous case, $\Delta T(h)$ error slightly grows beyond the cloud.

A marked influence upon the temperature profile reconstruction is exerted by changes in the scattering properties within the cloud layer as well. Figure 3c shows an example of $\Delta T(h)$ calculations for the cloud layer composed of a set of hexagonal columns and plates of different sizes and whose scattering properties are described by the average weighted scattering phase function $g(\vartheta)$.

Calculations of $g(\vartheta)$ for each particle type are performed by the method considered in Ref. 35. It has a greater asymmetry as compared to $g(\vartheta)$ used in the calculations shown in Figs. 3a and b. In this case, the $\Delta T(h)$ temperature reconstruction error also grows, both inside and outside the cloud. This is due to a higher multiple scattering level of the Raman signal component, which is supported by a high asymmetry of the scattering phase function of cloud particles.

Figure 4 shows the dependence of the $T(h)$ reconstruction accuracy on optical density of the cloud layer. In this example, the Raman signal is recorded in the lines of the anti-Stokes component at $\lambda_1 = 529.25$ and $\lambda_2 = 530.35$ nm.^{6,20}

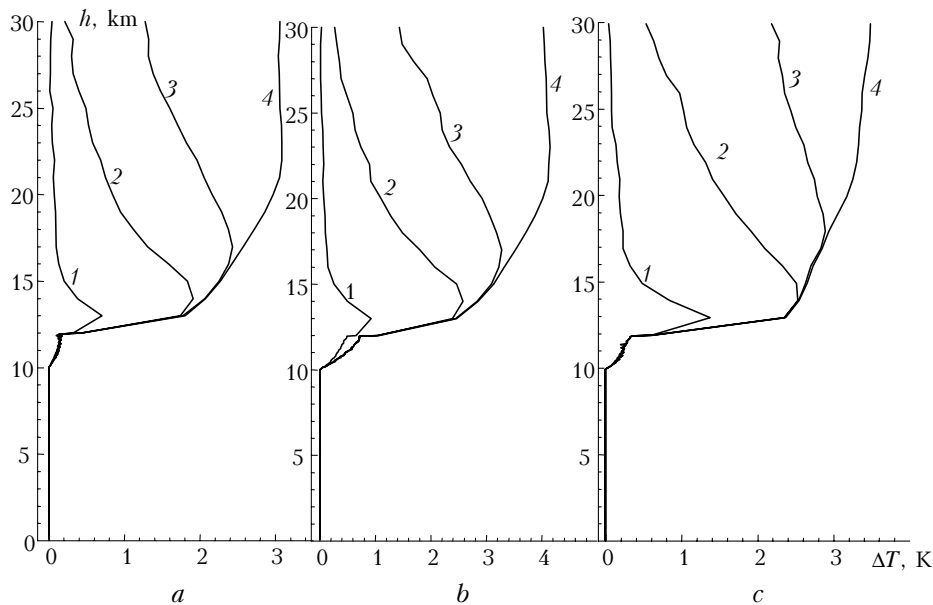


Fig. 3. Absolute error of the temperature profile $T(h)$ reconstruction for different optical situations: (a) calculation of $\Delta T(h)$ by $\sigma_a(h)$ corresponding to those in Fig. 2a; (b) Fig. 2b; (c) $\sigma_a(h)$ in Fig. 2a, but with a polydisperse cloud scattering phase function. Optical cloud thickness $\Delta\tau_{c1} = 0.5$. Curves 1–4 are calculated for $\varphi_d = 0.2; 0.4; 0.6$, and 1 mrad.

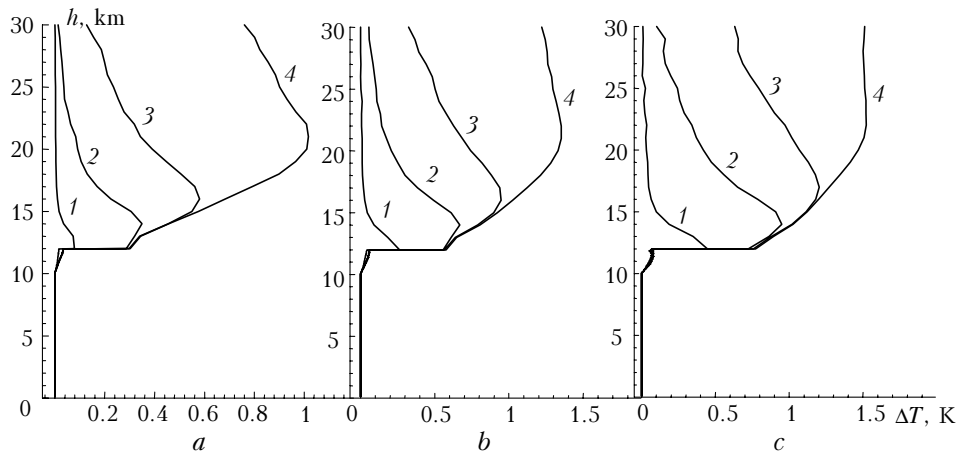


Fig. 4. Absolute $T(h)$ reconstruction error in the lines of the anti-Stokes signal branch at the wavelengths $\lambda_1 = 529.25$ and $\lambda_2 = 530.35$ nm depending on $\Delta\tau$ of the cloud layer; a , b , and c correspond to 0.2, 0.5, and 1.0; curves 1–4 – to the calculations for the receiving angles $\varphi_d = 0.2, 0.4, 0.6, 1.0$ mrad.

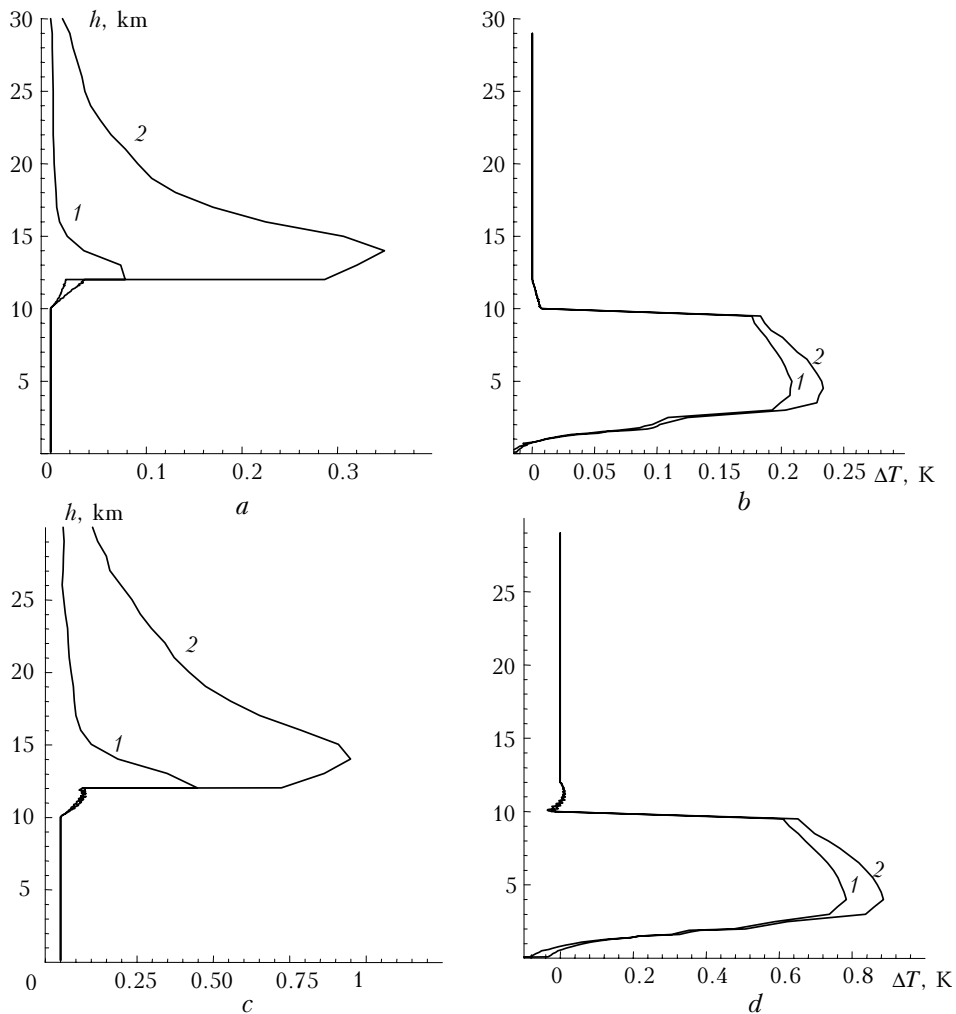


Fig. 5. Absolute sensing error $\Delta T(h)$ (in the lines from Fig. 4): a and c indicate ground-based lidar measurements; b and d refer to orbital lidar measurements; for a and b , $\Delta\tau_{Cl} = 0.2$; for c and d , $\Delta\tau_{Cl} = 1.0$. Curves 1 and 2 are calculated for $\varphi_d = 0.2$ and 0.4 mrad.

Figure 4 gives results for the cloud layers with the optical density $\Delta\tau_{Cl} = 0.2, 0.5$, and 1.0 , respectively. High $T(h)$ reconstruction accuracy is kept up to the cloud altitudes. Outside a cloud, $\Delta T(h)$ reaches its

maximum and then monotonically decreases. The error extent depends apparently on both the φ_d aperture sizes and the optical cloud layer density. For an optically thin cloud with $\Delta\tau_{Cl} \sim 0.2$, the maximal error level

depending on the receiving aperture varies from 0.1 to 1° (0.5–1.5° for a denser cloud with $\Delta\tau_{C1} \sim 1$). Comparing the calculation results illustrated in Figs. 3a and 4b, it should be noted that the reconstruction accuracy of the temperature profile for the same parameters of the cloud layer and receiving apertures decisively depends on a choice of spectral regions of the Raman lidar. Thus, at registration in two lines of the anti-Stokes RRS components ($\lambda_1 = 529.25$ and $\lambda_2 = 530.35$ nm), the $T(h)$ reconstruction accuracy is doubled comparative to that registered in the lines of anti-Stokes ($\lambda_1 = 530.35$ nm) and Stokes ($\lambda_2 = 534$ nm) RRS components. The reason is apparent and consists in different spectral behaviors of optical characteristics of the scattering medium.

The use of the orbital lidar systems becomes a routine for scientific research as is demonstrated in Ref. 32, therefore, we thought it pertinent to present calculations (Figs. 5b and d) for this lidar type.

To make the comparison with the ground-based measurements more convenient, data were calculated for the same geometrical and optical parameters that are indicated in Fig. 4. The only distinction concerns the altitude of the lidar system location. The lidar is 700 km away from the Earth's surface and registers signals coming from the 30 km near-surface atmospheric layer.

Figure 5 gives calculation results for the ground-based (a, c) and orbital (b, d) lidars. Calculations show that, when sensing by the orbital lidar, $T(h)$ profile reconstruction accuracy for the receiving angle $\varphi_d = 0.4$ mrad is nearly the same for both sensing schemes. For $\varphi_d = 0.2$ mrad and the ground-based sensing scheme, $\Delta T(h)$ is somewhat lower beyond the cloud layer. In the first case, a greater scattering volume for the orbital lidar is compensated by a lower level of the singly scattered Raman signal in the upper atmospheric layers. For a smaller angle, the compensation is insufficient, and $T(h)$ reconstruction error, when sensing by the ground-based lidar, is a bit lower, especially at a low optical density of the cloud layer ($\Delta\tau_{C1} = 0.2$ in the example given in Figs. 5a and b). At orbital sensing, to lessen optical size of the scattering volume, small receiving angles of about 0.1–0.2 mrad are preferred, as a rule.

We do not consider estimates of other factors influencing the $\Delta T(h)$ error, such as quantum noise statistics, since they were comprehensively discussed in Refs. 5, 7, 15, 33, 49.

Model estimates of vertical humidity profiles in the multiple scattering conditions

The earliest studies of water vapor spatial distribution in the atmosphere performed with the use of the Raman lidars were reported in Refs. 45 and 46. A thorough review of modern methods and lidar sensing results of vertical humidity profiles including Raman techniques was made by V. Wulfmeyer and C. Walter.⁴⁷ The commonly accepted methods of

retrieving information on vertical humidity distribution is based mostly on quantitative interpreting of the H₂O vapor backscattering signals normalized relative to the similar signals of N₂ or O₂. Therewith, it is accepted that all the signals are conditioned by the single scattering, i.e., meet the location equation of type (7). The ratio of the lidar signals in the assumption of Eq. (7) at the frequencies of the chosen vibrational transitions of the Raman scattering of H₂O vapor molecules and, for example, N₂, results in a simple estimate of the H₂O vapor mixing ratio, $m_{\text{H}_2\text{O}}(h)$, which is one of most important characteristics of the atmospheric state.³¹ Actually,

$$\frac{P_{\text{H}_2\text{O}}(h, \nu_{\text{H}_2\text{O}})}{P_{\text{N}_2}(h, \nu_{\text{N}_2})} = C_{\text{R}}^* \frac{N_{\text{H}_2\text{O}}(h) \frac{d\sigma_{\text{R}}^{\text{H}_2\text{O}}}{d\Omega}}{N_{\text{N}_2}(h) \frac{d\sigma_{\text{R}}^{\text{N}_2}}{d\Omega}} \times \exp \left\{ - \int_0^h [\sigma(h', \nu_{\text{H}_2\text{O}}) - \sigma(h', \nu_{\text{N}_2})] dh' \right\}, \quad (15)$$

where C_{R}^* is the instrumental constant accounting for the relative transmission and optical efficiency of the receiving channels at the frequencies $\nu_{\text{H}_2\text{O}}$ and ν_{N_2} . By definition³¹

$$m_{\text{H}_2\text{O}} = \frac{\mu_{\text{H}_2\text{O}} N_{\text{H}_2\text{O}}(h)}{\mu_{\text{N}_2} N_{\text{N}_2} / 0.78}, \quad (16)$$

where $\mu_{\text{H}_2\text{O}}$, μ_{N_2} stand for molecular weights of H₂O vapor and dry air, respectively, wherefrom, taking into account Eq. (15), it follows that

$$m_{\text{H}_2\text{O}}(h) = K^* \frac{P_{\text{H}_2\text{O}}(h, \nu_{\text{H}_2\text{O}})}{P_{\text{N}_2}(h, \nu_{\text{N}_2})} \Delta\eta(h, \nu_{\text{H}_2\text{O}}, \nu_{\text{N}_2}), \quad (17)$$

where K^* is the integrated calibration constant that includes the ratio of the differential scattering cross sections;

$$\Delta\eta(h, \nu_{\text{H}_2\text{O}}, \nu_{\text{N}_2}) = \exp \left\{ - \int_0^h [\sigma(h', \nu_{\text{H}_2\text{O}}, \nu_{\text{N}_2}) - \sigma(h', \nu_{\text{N}_2})] dh' \right\} \quad (18)$$

is a difference of atmospheric transmission in the registration channels $\nu_{\text{H}_2\text{O}}$ and ν_{N_2} being a poorly controlled complementary source of errors. Since in *in situ* measurements it is assumed that $\Delta\eta(h, \nu_{\text{H}_2\text{O}}, \nu_{\text{N}_2}) = 1$, then the calibration constant K^* is determined for every lidar from the corresponding measurements.⁴⁸ In our numerical experiment, this constant is estimated based on the model profile $m_{\text{H}_2\text{O}}^*(h)$ using, for example, the data of Ref. 34. In reconstruction of vertical profiles $m_{\text{H}_2\text{O}}(h)$, the influence of multiple scattering is taken into account through using the correction factor of the form Eq. (12). Besides, we evaluate the bias $\Delta m_{\text{H}_2\text{O}}(h)$

resulting from possible variations of $\Delta\eta(h, v_{\text{H}_2\text{O}}, v_{\text{N}_2})$ values because of unknown spectral behavior of $\sigma(h, v)$.

A more usable meteorological parameter characterizing the spatial atmospheric water vapor distribution is the relative humidity $f_\omega(h)$, which, as we know, is connected with distribution of the mixing ratio $m_{\text{H}_2\text{O}}(h)$ and the temperature $T(h)$:

$$f_\omega(h) = \frac{p(h)m_{\text{H}_2\text{O}}(h)}{0.622 + m_{\text{H}_2\text{O}}(h)} \exp\left[-\frac{17.84T'(h)}{M_\omega + T'(h)}\right], \quad (19)$$

where

$$T'(h) = T(h) - 273 \text{ K};$$

$$M_\omega = \begin{cases} 245.4 & \text{at } T(h) < 273 \text{ K} \\ 234.2 & \text{at } T(h) > 273 \text{ K}; \end{cases} \quad (20)$$

$p(h)$ is the partial pressure of H_2O vapor. Dependence of $f_\omega(h)$ on the ambient temperature is the second source of errors, which also must be regarded.

Relative errors in reconstruction of vertical distribution of the mixing ratio $\delta m_{\text{H}_2\text{O}}(h)$ in different sensing conditions are shown in Fig. 6. The results are given for the receiving device aperture of $\varphi_d = 0.2$ mrad.

Figure 6a shows the relative error profile $\delta m_{\text{H}_2\text{O}}(h)$ for the cloudless atmosphere; the aerosol profile $\sigma_a(h)$ corresponds to Fig. 2a in Ref. 33.

At the end of the sensing path, the relative error reaches $\sim 2.5\%$. Taking into account that in the considered situation the lidar signal is formed mainly due to the single scattering,⁴² we can state that the relative reconstruction error in $m_{\text{H}_2\text{O}}(h)$ is determined by $\Delta\eta(h, v_{\text{H}_2\text{O}}, v_{\text{N}_2})$ variation along the sensing path. Figures 6b–d illustrate the influence of the cloud layer with the optical density $\Delta\tau_{\text{Cl}} = 0.2, 0.5, 1.0$, respectively, in the mentioned altitude interval onto the $m_{\text{H}_2\text{O}}(h)$ reconstruction accuracy.

In the presence of the cloud layer, the relative error is formed already due to two components: the multiply scattered component in the lidar signal and $\Delta\eta(h, v_{\text{H}_2\text{O}}, v_{\text{N}_2})$ variations along the sensing path. The $\delta m_{\text{H}_2\text{O}}(h)$ reaches its maximum beyond the cloud layer, varying from 5 to 20% depending on τ of the cloud. With the altitude, its value decreases, and starting from some altitudes, depending on the optical cloud density, it becomes stable.

The relative reconstruction error of the relative humidity $\delta f_\omega(h)$ is presented in Fig. 7.

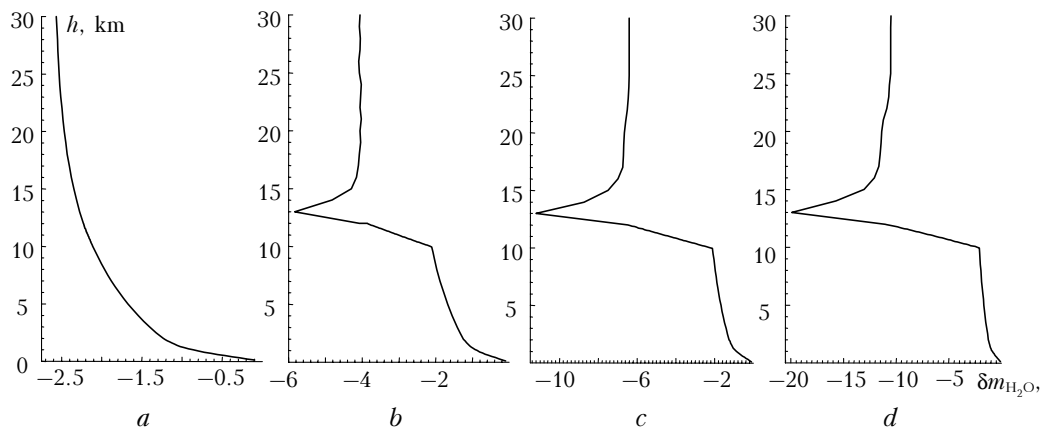


Fig. 6. The relative reconstruction error of the mixing ratio $m_{\text{H}_2\text{O}}(h)$ depending on the optical cloud layer thickness $\Delta\tau_{\text{Cl}}$: 0 (a); 0.2 (b); 0.5 (c); and 1.0 (d). Calculations are made for the receiving angle $\varphi_d = 0.2$ mrad.

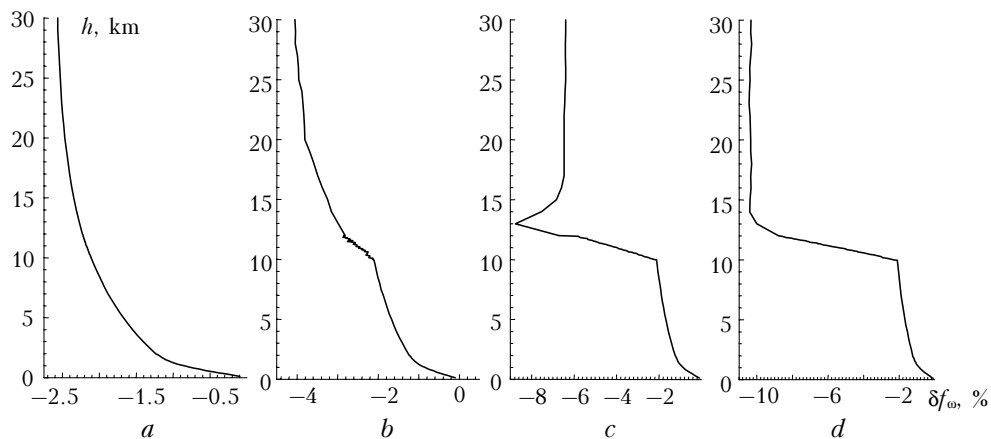


Fig. 7. The relative reconstruction error in $f_\omega(h)$ depending on the optical cloud layer thickness $\Delta\tau_{\text{Cl}}$: 0 (a); 0.2 (b); 0.5 (c); and 1.0 (d). The receiving angle $\varphi_d = 0.2$ mrad.

The calculations were performed both for the clear atmosphere (Fig. 7a) and cloud layers (Figs. 7b–d) with the same optical densities as in Fig. 6.

The temperature profile $T(h)$, required to reconstruct the relative humidity, was previously reconstructed from the model calculations of Raman sensing in the anti-Stokes ($\lambda = 530.3$ nm) and Stokes ($\lambda = 535.1$ nm) signal branches. The reconstruction accuracy for $f_{\omega}(h)$ (Fig. 7a) like in reconstruction of the mixing ratio is determined only by variation of $\Delta\eta(h, v_{\text{H}_2\text{O}}, v_{\text{N}_2})$ along the sensing path. In this case, the multiply scattered component in the lidar signal and the temperature profile reconstructed from its model value are insignificant. In the presence of a cloud layer, the accuracy of the relative humidity reconstruction is illustrated in Figs. 7b–d, wherefrom it follows that the maximum error $\delta f_{\omega}(h)$ varies approximately from 3 to 10% with increase of $\Delta\tau_{C1}$ of the cloud layer. For a denser cloud ($\Delta\tau_{C1} \sim 1$), the maximum value of the relative error is kept up to the end of the sensing path.

It must be noted that in reconstruction of the relative humidity, apart from the above two error sources, there is another one connected with the error of the temperature profile $T(h)$ reconstruction. Comparison of the calculation results of $\delta f_{\omega}(h)$ for the ground-based and orbital Raman lidar schemes is shown in Fig. 8.

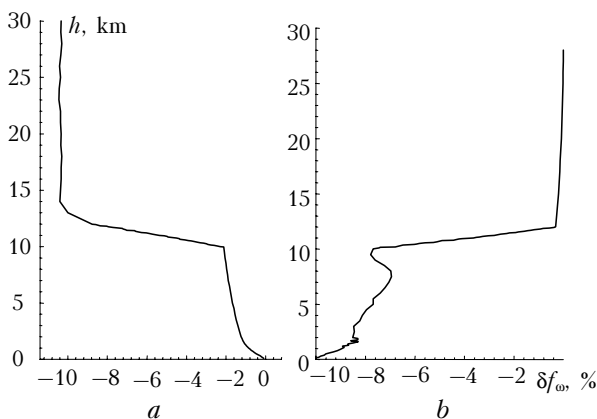


Fig. 8. The relative reconstruction error in $f_{\omega}(h)$ at sensing by the ground-based (a) and orbital (b) lidars; $\Delta\tau_{C1} = 1.0$; $\varphi_d = 0.2$ mrad.

It is obvious that the level of $\delta f_{\omega}(h)$ for the orbital sensing scheme is close to zero in the altitude interval beginning from the top boundary of the specified atmospheric layer up to the cloud layer altitude. At the bottom cloud boundary, it is also somewhat lower. The reason is obvious and connected with the low optical density of the upper atmospheric layer that favors minimal levels of all types of error that determine the reconstruction accuracy $\delta f_{\omega}(h)$. Beyond the cloud, $\delta f_{\omega}(h)$ grows rapidly and reaches approximately the same level as beyond the cloud layer in a ground-based scheme.

In a recent work,⁵⁰ the results of experimental measurements of vertical temperature and humidity

distribution by the methods of vibrational-rotational Raman spectroscopy are presented. The results obtained for thin cirrus clouds are in a good quantitative agreement with the above estimates. Deviations of the $\Delta T(h)$ temperature do not exceed several degrees, however, variations of the relative humidity $\delta f_{\omega}(h)$ in the aerosol inversion region reach several tens of percent.

Conclusions

We present the results of numerical investigations of limits of application of the vibrational-rotational Raman spectroscopy methods for the lidar sensing of temperature and humidity in a cloudy atmosphere. All known methods of vibrational-rotational Raman spectroscopy are based on the use of single-scattering signals $P^{SS}(h)$. The essence of our numerical experiment consists in substitution into the known inversion formulas of the “real” $P^{MS}(h)$ signals obtained via exact solution of the adequate transfer equation and determination of arising deviations of $\Delta T(h)$, $\delta m_{\text{H}_2\text{O}}(h)$, and $\delta f_{\omega}(h)$.

The obtained estimates of possible variations $\Delta T(h)$ and $\delta f_{\omega}(h)$ occurring due to multiple scattering noise do not contradict the known data (few in number) on experimental measurements under conditions of thin clouds.

Special features of accumulation of errors of meteorological parameter reconstruction in the ground-based and orbital sensing schemes are considered.

Acknowledgments

This work is accomplished in the framework of the Program 1.4 SB RAS-10 of the Presidium of the Russian Academy of Sciences under financial support of the Russian Foundation for Basic Research (grant No. 03–05–64228).

References

1. G.M. Krekov, S.I. Kavkyanov, and M.M. Krekova, *Interpreting the Signals of Optical Sensing of the Atmosphere* (Nauka, Novosibirsk, 1987), 185 pp.
2. D.V. Pozdnyakov, A.V. Lyaskovsky, H. Grassl, and L. Petterson, *Issled. Zemli iz Kosmosa*, No. 5, 3–15 (2000).
3. S. Sathyendranath and T. Platt, *Appl. Opt.* **37**, 2216–2227 (1998).
4. G.M. Krekov and M.M. Krekova, *Atmos. Oceanic Opt.* **17**, No. 10, 745–752 (2004).
5. D.N. Whiteman, *Appl. Opt.* **42**, 2571–2608 (2003).
6. G. Pappalardo, A. Amodea, M. Pandolf, U. Wandinger, A. Ansmann, J. Bosenberg, V. Matthias, and V. Amiridis, *Appl. Opt.* **43**, 5370–5385 (2004).
7. V.V. Zuev, A.V. Elnikov, and V.D. Burlakov, *Laser Sensing of the Middle Atmosphere* (Rasko, Tomsk, 2002), 352 pp.
8. S.H. Melfi, D.N. Whiteman, R.A. Ferrare, *J. Appl. Meteorol.* **28**, 789–806 (1989).
9. R.A. Ferrare, S.H. Melfi, D.N. Whiteman, and K.D. Evans, *Geophys. Res. Lett.* **19**, 1599–1602 (1992).

10. S.V. Merkurjev, V.E. Privalov, and V.G. Shemanin, *Pis'ma Zh. Teor. Fiz.* **26**, 45–49 (2000).
11. D. Muller, U. Wandinger, and A. Ansmann, *Appl. Opt.* **38**, 2358–2368 (1999).
12. A. Ansmann, M. Riebesell, C. Weitkamp, E. Voss, W. Lachmann, and W. Michaelis, *Appl. Opt.* **55**, 18–28 (1992).
13. C.M.R. Platt, R.T. Austin, S.A. Young, and A.J. Heumsfeld, *J. Atmos. Sci.* **59**, 3145–3173 (2002).
14. K.N. Liou, *Mon. Weather Rev.* **114**, 1167–1195 (1986).
15. V.M. Zakharov, ed., *Space Laser Sensing* (Gidrometeoizdat, Leningrad, 1988), 150 pp.
16. A.J. Heymsfield and C.M.R. Platt, *J. Atmos. Sci.* **41**, 846–855 (1984).
17. E.D. Hinkley, ed., *Laser Monitoring of the Atmosphere* (Springer Verlag, New York, 1976).
18. V.E. Zuev and V.V. Zuev, *Remote Optical Sensing of the Atmosphere* (Gidrometeoizdat, Leningrad, 1992), 232 pp.
19. G. Vangham, D.P. Wareing, S.J. Pepler, L. Thomas, and V. Mitev, *Appl. Opt.* **32**, 2758–2764 (1993).
20. A. Behrendt and J. Reichardt, *Appl. Opt.* **39**, 1372–1378 (2000).
21. I. Mattis, A. Ansmann, D. Althansen, V. Jaenisch, U. Wandinger, D. Muller, Yu.F. Arshinov, S.M. Bobrovnikov, and I.B. Serikov, *Appl. Opt.* **41**, 6451–6462 (2002).
22. G.M. Krekov, I.E. Naats, and V.N. Skorinov, in: *Atmospheric Laser Sensing Issues* (Nauka, Novosibirsk, 1976), pp. 69–73.
23. V.E. Zuev, G.M. Krekov, I.E. Naats, and V.N. Skorinov, *Izv. Akad. Nauk SSSR, Fiz. Atmos. Okeana* **11**, 1326–1330 (1975).
24. V.M. Zakharov and O.K. Kostko, *Meteorological Laser Location* (Gidrometeoizdat, Leningrad, 1977), 222 pp.
25. Yu.F. Arshinov and S.A. Danichkin, in: *Optical Wave Propagation in the Atmosphere* (Nauka, Novosibirsk, 1975), pp. 169–173.
26. Yu.F. Arshinov, S.M. Bobrovnikov, V.E. Zuev, and V.M. Mitev, *Appl. Opt.* **22**, 2984–2990 (1983).
27. J. Cooney, *J. Appl. Meteorol.* **11**, 108–112 (1972).
28. S. Kelikh, *Nonlinear Molecular Optics* (Nauka, Moscow, 1981), 672 pp.
29. H. Shretter and H. Klekner, in: *Raman Light Scattering Cross Sections in Liquids and Gases* [Russian translation] (Mir, Moscow, 1983), pp. 154–202.
30. M.A. Buldakov, I.I. Matrosov, and V.N. Cherepanov, *Atmos. Oceanic Opt.* **16**, 98–102 (2003).
31. L.G. Matveev, *General Meteorology. Atmospheric Physics* (Gidrometeoizdat, Leningrad, 1976), 639 pp.
32. R.H. Couch, C.W. Rowland, K.S. Ellis, M.P. Blythe, C.P. Reagan, and M.R. Koch, *Opt. Eng.* **30**, 88–98 (1991).
33. G.M. Krekov and R.F. Rakhimov, *Optical Models of Atmospheric Aerosol* (Tomsk Branch of SB AS USSR, Tomsk, 1986), 294 pp.
34. V.E. Zuev and V.S. Komarov, *Statistical Models of Temperature and Gas Components of the Atmosphere* (Gidrometeoizdat, Leningrad, 1986), 264 pp.
35. G.M. Krekov, M.M. Krekova, D.N. Romashov, and V.S. Shamanaev, *Izv. Vyssh. Uchebn. Zaved., Fiz.* **44**, No. 11, 56–66 (2001).
36. G.I. Marchuk, ed., *Monte Carlo Methods in Atmospheric Optics* (Springer-Verlag, Berlin, Hiedelberg, 1980), 206 pp.
37. U. Wandinger, *Appl. Opt.* **37**, 417–427 (1998).
38. M. Wengenmayer, A.Y.S. Cheng, P. Volger, and U.G. Oppel, *Proc. SPIE* **5059**, 200–211 (2003).
39. J. Reichardt, *Appl. Opt.* **39**, 6058–6071 (2000).
40. P. Brusaglioni, M. Gai, and A. Ismaelli, in: *Proc. of MUSCLE 10* (Florence, 1999), pp. 206–212.
41. D. Deirmendjian, *Electromagnetic Scattering on Spherical Polydispersions* (American Elsevier, New York 1969).
42. G.G. Matvienko, G.M. Krekov, and M.M. Krekova, in: *Proc. of MUSCLE 10* (Florence, 1999), pp. 157–164.
43. L.R. Bissonette, P. Brusaglioni, A. Ismaelli, G. Zaccanti, A. Cohen, J. Banayahy, M. Kleiman, S. Egert, C. Flesia, and A.V. Starkov, *J. Appl. Phys. B* **60**, 355–362 (1995).
44. A. Ansmann, Yu. Arshinov, S. Bobrovnikov, I. Mattis, I. Serikov, and U. Wandinger, *Proc. SPIE* **3583**, 491–497 (1998).
45. S.H. Melfi, J.D. Lawrence, and M.P. McCormick, *Appl. Phys. Lett.* **15**, 295–297 (1969).
46. J.A. Conney, *J. Appl. Meteorol.* **9**, 182–184 (1970).
47. V. Wulfmeyer and C. Walter, *Appl. Opt.* **40**, 5304–5336 (2001).
48. V. Sherlock, A. Hauchecorne, and J. Lenoble, *Appl. Opt.* **38**, 5816–5837 (1999).
49. B. Lasarotto, M. Frioud, G. Larchevegne, V. Mitev, P. Quaqlia, and V. Simeonov, *Appl. Opt.* **40**, 2985–2997 (2001).
50. R. Marchese, P. Girolomo, B.B. Demoz, and D. Whiteman, in: *Proc. 22nd Intern. Laser Radar Conf.* (Matera, 2004), pp. 455–458.